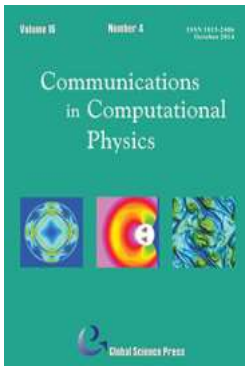

A Compact Third-Order Gas-Kinetic Scheme for Compressible Euler and Navier-Stokes Equations

Liang Pan and Kun Xu

Communications in Computational Physics / Volume 18 / Issue 04 / October 2015, pp 985 - 1011
DOI: 10.4208/cicp.141214.140715s, Published online: 15 October 2015

Commun. Comput. Phys.
doi: 10.4208/cicp.141214.140715s

Vol. **18**, No. 4, pp. 985-1011
October 2015

A Compact Third-Order Gas-Kinetic Scheme for Compressible Euler and Navier-Stokes Equations

Liang Pan and Kun Xu*

Department of mathematics, Hong Kong University of Science and Technology, Clear Water Bay, Kowloon, Hong Kong.

Received 14 December 2014; Accepted (in revised version) 14 July 2015

Abstract. In this paper, a compact third-order gas-kinetic scheme is proposed for the compressible Euler and Navier-Stokes equations. The main reason for the feasibility to develop such a high-order scheme with compact stencil, which involves only neighboring cells, is due to the use of a high-order gas evolution model. Besides the evaluation of the time-dependent flux function across a cell interface, the high-order gas evolution model also provides an accurate time-dependent solution of the flow variables at a cell interface. Therefore, the current scheme not only updates the cell averaged conservative flow variables inside each control volume, but also tracks the flow variables at the cell interface at the next time level. As a result, with both cell averaged and cell interface values, the high-order reconstruction in the current scheme can be done compactly. Different from using a weak formulation for high-order accuracy in the Discontinuous Galerkin method, the current scheme is based on the strong solution, where the flow evolution starting from a piecewise discontinuous high-order initial data is precisely followed. The cell interface time-dependent flow variables can be used for the initial data reconstruction at the beginning of next time step. Even with compact stencil, the current scheme has third-order accuracy in the smooth flow regions, and has favorable shock capturing property in the discontinuous regions. It can be faithfully used from the incompressible limit to the hypersonic flow computations, and many test cases are used to validate the current scheme. In comparison with many other high-order schemes, the current method avoids the use of Gaussian points for the flux evaluation along the cell interface and the multi-stage Runge-Kutta time stepping technique. Due to its multidimensional property of including both derivatives of flow variables in the normal and tangential directions of a cell interface, the viscous flow solution, especially those with vortex structure, can be accurately captured. With the same stencil of a second order scheme, numerical tests demonstrate that the current scheme is as robust as well-developed second-order shock capturing schemes, but provides more accurate numerical solutions than the second order counterparts.

AMS subject classifications: 76P05, 76N15

Key words: Third-order gas-kinetic scheme, compact reconstruction, Navier-Stokes solutions.

*Corresponding author. *Email addresses:* panliangjlu@sina.com (L. Pan), makxu@ust.hk (K. Xu)

1 Introduction

Most computational fluid dynamics methods used in practical applications are second-order methods. They are generally robust and reliable. For the same computing cost, the high-order methods (order ≥ 3) can provide more accurate solutions, but they are less robust and more complicated. There has been a surge of research activities on the development of high-order methods for solving the Euler and Navier-Stokes equations. At the current stage, many high-order numerical methods have been developed, including discontinuous Galerkin (DG), spectral volume (SV), spectral difference (SD), correction procedure using reconstruction (CPR), essential non-oscillatory (ENO), and weighted essential non-oscillatory (WENO), etc. The DG scheme was first proposed in [29] to solve the neutron transport equation. A major development of the DG method was carried out by Cockburn et al. [4, 5] to solve the hyperbolic conservation laws. In the DG method, high-order accuracy is achieved by means of high-order polynomial approximation within each element rather than by means of wide stencils, and Runge-Kutta method is used for the time discretization. Because only flow interaction from neighboring elements is included, it becomes compact and efficient in the application on complex geometry. Recently, a correction procedure via reconstruction framework (CPR) was developed by Wang et al. [12, 36]. This method was originally developed to solve one-dimensional conservation laws, under the name of flux reconstruction [14, 15]. Under lifting collocation penalty, the CPR framework was extended to two-dimensional triangular and mixed grids. The CPR formulation is based on a nodal differential form, with an element-wise continuous polynomial solution space. By choosing certain correction functions, the CPR framework can unify several well known methods, such as the DG, SV [23] and SD [35] methods and lead to simplified versions of these methods, at least for linear equations. The CPR method is compact because only immediate face neighbors play a role in updating the solutions in the current cell. Therefore, the complexity of implementation can be reduced, especially for the simulation with unstructured mesh. The main problem for the above DG-type schemes are the robustness of the method, especially in the cases with discontinuities. It is certainly true that the use of limiters can save the DG methods in the flow computations with discontinuities. But, the DG method is extremely sensitive to the limiters, because it is hard to distinguish the continuous or discontinuous solution in a computation, especially with the changing of cell size. Sometimes, the DG method can mysteriously get failure in a computation without clear reasons. Therefore, to pick up the trouble cells beforehand becomes a practice in the DG method. After so many years' research on the DG method, it gives perfect results for the continuous flow simulations, but seems have physical problem in its weak formulation in the discontinuous case.

The ENO scheme was proposed by Harten et al. [9, 31] and successfully applied to solve hyperbolic conservation laws and other convection dominated problems. Following the ENO scheme, WENO scheme [10,17,22] was further developed. ENO scheme uses the smoothest stencil among several candidates to approximate the numerical fluxes at cell interface for high-order accuracy. At the same time, it avoids spurious oscillations

near discontinuities. Meanwhile, WENO scheme is a convex linear combination of lower order reconstructions to obtain a higher order approximation. WENO scheme improves upon ENO scheme in robustness, smoothness of fluxes, steady-state convergence, provable convergence properties, and more efficiency. However, in both ENO and WENO schemes, large stencils in the high-order reconstruction and Runge-Kutta time stepping are used, especially for the multi-dimensional unstructured meshes [17]. There are also many other high-order schemes which can be found in the literature. The DG method for its compactness and the WENO for the reconstruction are mostly related to the current research for the development of high-order compact gas-kinetic scheme.

The gas-kinetic scheme (GKS) based on the Bhatnagar-Gross-Krook (BGK) model [1–3] has been developed systematically for the compressible flow computations [16, 19, 39,40,43]. The gas-kinetic scheme presents a gas evolution process from a kinetic scale to a hydrodynamic scale, where both inviscid and viscous fluxes are recovered from moments of a single time-dependent gas distribution function. In discontinuous shock region, the kinetic scale physics, such as particle free transport through upwinding, takes effect to construct a crisp and stable shock transition. The highly non-equilibrium of the gas distribution function in the discontinuous region provides a physically consistent mechanism for the construction of numerical shock structure. In smooth flow region, the hydrodynamic scale physics corresponding to the multi-dimensional central difference discretization will contribute mainly in the kinetic flux function, and accurate Navier-Stokes solution can be obtained once the flow structure is well resolved. Based on the unified coordinate transformation, a moving-mesh gas-kinetic scheme has been developed [18, 28]. With the discretization of particle velocity space, a unified gas-kinetic scheme (UGKS) has been developed for the flow study in entire Knudsen number regimes from rarefied to continuum ones [13, 26, 41]. Recently, with the incorporation of high-order initial reconstruction, high-order gas-kinetic schemes for the inviscid and viscous flows have been proposed in [20, 24, 25]. The flux evaluation in the scheme is based on the time evolution of flow variables from an initial piece-wise discontinuous polynomials around a cell interface, where high-order spatial and temporal derivatives of a gas distribution function are coupled nonlinearly.

In this paper, a compact third-order gas-kinetic scheme is proposed for the compressible Euler and Navier-Stokes equations. Different from the Riemann solver with first-order dynamics [8, 34], the gas-kinetic scheme uses a time evolution solution for the flux evaluation from the initial piecewise discontinuous polynomials. Besides the evaluation of the time-dependent flux function across a cell interface, the high-order gas evolution model also provides an accurate time-dependent solution of the flow variables at a cell interface. Following the previous work for the second-order compact gas-kinetic scheme [38], the current study concentrates on the construction of a third-order one. The reason for the compactness of the scheme is that it not only updates the cell averaged conservative flow variables inside each control volume, but also provides the flow variables at the cell interface at the next time level. As a result, both cell averaged and cell interface values can be used for the high-order initial data reconstruction. The weak for-

mulation of DG method doesn't have such a time accurate cell interface value. The strong solution, which follows the time evolution of flow variables starting from a piecewise discontinuous high-order initial data, is required in the construction of the current scheme. Due to the additional cell interface values, a compact stencil with WENO-type reconstruction can be used in the current high-order scheme. The current scheme not only has third-order accuracy in the smooth flow regions, but also has favorable shock capturing property in the discontinuous cases. In comparison with other high-order schemes, the current method doesn't use the Gaussian points for the flux evaluation along the cell interface and the multi-stage Runge-Kutta technique.

This paper is organized as follows. Section 2 introduces the BGK equation and the multi-dimensional high-order gas-kinetic solver. Section 3 presents the reconstruction with compact stencil. Section 4 presents numerical examples to validate the current scheme. The last section is the conclusion.

2 BGK equation and high-order gas-kinetic solver

2.1 BGK equation

The two-dimensional BGK equation can be written as

$$f_t+uf_x+vf_y=\frac{g-f}{\tau}, \tag{2.1}$$

where f is the gas distribution function, g is the corresponding equilibrium state and τ is the collision time. The collision term satisfies the compatibility condition

$$\int \frac{g-f}{\tau}\psi d\Xi=0, \tag{2.2}$$

where $\psi=(1,u,v,\frac{1}{2}(u^2+v^2+\xi^2))$, $d\Xi=dudvd\xi^1\cdots d\xi^K$, K is the number of internal freedom, i.e. $K=(4-2\gamma)/(\gamma-1)$ for two-dimensional flows and γ is the specific heat ratio.

Based on the Chapman-Enskog expansion of the BGK model, the Euler and Navier-Stokes, Burnett, and Super-Burnett equations can be derived [3, 27, 39]. In the smooth region, the gas distribution function can be expanded as

$$f=g-\tau D_{\mathbf{u}}g+\tau D_{\mathbf{u}}(\tau D_{\mathbf{u}})g-\tau D_{\mathbf{u}}[\tau D_{\mathbf{u}}(\tau D_{\mathbf{u}})g]+\cdots,$$

where $D_{\mathbf{u}}=\frac{\partial}{\partial t}+\mathbf{u}\cdot\nabla$. By truncating different orders of τ, the corresponding macroscopic equations can be derived. For the Euler equations, the zeroth order truncation is taken, i.e. $f=g$. For the Navier-Stokes equations, the first order truncation is

$$f=g-\tau(ug_x+vg_y+g_t). \tag{2.3}$$

Based on the higher order truncations, the Burnett and super-Burnett equations can be obtained.

Taking moments of the BGK equation (2.1) and integrating with respect to time and space, the finite volume scheme can be obtained

$$W_{ij}^{n+1}=W_{ij}^{n}+\frac{1}{\Delta x\Delta y}\int_{t^n}^{t^{n+1}}\int_{-\frac{\Delta y}{2}}^{\frac{\Delta y}{2}}[F_{i-1/2,j}(t,y)-F_{i+1/2,j}(t,y)]dydt$$
$$+\frac{1}{\Delta x\Delta y}\int_{t^n}^{t^{n+1}}\int_{-\frac{\Delta x}{2}}^{\frac{\Delta x}{2}}[G_{i,j-1/2}(t,x)-G_{i,j+1/2}(t,x)]dxdt, \tag{2.4}$$

where $W=(\rho,\rho U,\rho V,\rho W,\rho E)$ are the conservative variables, and $F_{i+1/2,j}(t,y)$ and $G_{i,j+1/2}(t,x)$ are time-dependent numerical fluxes in the x and y directions, which can be obtained by taking moments of the gas distribution function at the cell interface,

$$F_{i+1/2,j}(t,y)=\int u\psi f(x_{i+1/2},y,t,u,v,\xi)d\Xi.$$

Similarly, the fluxes $G_{i,j+1/2}$ in the y direction can be obtained.

2.2 High-order gas-kinetic solver

To construct numerical fluxes, the integral solution of the BGK equation (2.1) at the cell interface can be written as

$$f(x_{i+1/2},y,t,u,v)=\frac{1}{\tau}\int_0^t g(x',y',t',u,v)e^{-(t-t')/\tau}dt'+e^{-t/\tau}f_0(-ut,y-vt), \tag{2.5}$$

where $x_{i+1/2}=0$ is the location of cell interface, $x_{i+1/2}=x'+u(t-t')$ and $y=y'+v(t-t')$ are the particle trajectories. In the above integral solution, the initial term f_0 accounts for the free transport mechanism along particle trajectories, which represents the kinetic scale physics. The integration of equilibrium state along the particle trajectories represents the accumulating effect of an equilibrium state, which is related to the hydrodynamic scale flow physics. The flow behavior at the cell interface depends on the ratio of time step and local particle collision time $\Delta t/\tau$ [39].

To construct a multidimensional third-order gas-kinetic solver, the following notations are introduced firstly

$$a_1=(\partial g/\partial x)/g, a_2=(\partial g/\partial y)/g, A=(\partial g/\partial t)/g, B=(\partial A/\partial t),$$
$$d_{11}=(\partial a_1/\partial x), d_{12}=(\partial a_1/\partial y)=(\partial a_2/\partial x), d_{22}=(\partial a_2/\partial y),$$
$$b_1=(\partial a_1/\partial t)=(\partial A/\partial x), b_2=(\partial a_2/\partial t)=(\partial A/\partial y),$$

where g is an equilibrium state. The dependence of these coefficients on particle velocity can be expanded as the following form [40]

$$a_1=a_{11}+a_{12}u+a_{13}v+a_{14}\frac{1}{2}(u^2+v^2+\xi^2),$$
$$\vdots$$
$$B=B_1+B_2u+B_3v+B_4\frac{1}{2}(u^2+v^2+\xi^2).$$

For the kinetic part of the integral solution Eq. (2.5), the gas distribution function is constructed as

$$f_0 = f_0^l(x,y,u,v)H(x) + f_0^r(x,y,u,v)(1-H(x)), \tag{2.6}$$

where $H(x)$ is the Heaviside function, f_0^l and f_0^r are the initial gas distribution functions on both sides of a cell interface, which have one-to-one correspondence with the initially reconstructed polynomials of macroscopic flow variables on both sides of the cell interface. To construct a third-order scheme, the Taylor expansion for the gas distribution function in space at $(x,y)=(0,0)$ is expressed as

$$f_0^k(x,y) = f_G^k(0,0) + \frac{\partial f_G^k}{\partial x}x + \frac{\partial f_G^k}{\partial y}y + \frac{1}{2}\frac{\partial^2 f_G^k}{\partial x^2}x^2 + \frac{\partial^2 f_G^k}{\partial x\partial y}xy + \frac{1}{2}\frac{\partial^2 f_G^k}{\partial y^2}y^2, \tag{2.7}$$

where $k=l,r$. For the Euler equations, $f_G^k = g_k$ and the kinetic part of Eq. (2.5) can be obtained. For the Navier-Stokes equations, according to Eq. (2.3) and the notations introduced above, the gas distribution function is

$$f_G^k = g_k - \tau(a_{1k}u + a_{2k}v + A_k)g_k.$$

Substituting it into Eq. (2.7), the kinetic part of the integral solution Eq. (2.5) is written as

$$\begin{aligned}
&e^{-t/\tau}f_0^k(-ut,y-vt,u,v)\\
=&C_7g_k[1-\tau(a_{1k}u+a_{2k}v+A_k)]\\
&+C_8g_k[a_{1k}u-\tau((a_{1k}^2+d_{11k})u^2+(a_{1k}a_{2k}+d_{12k})uv+(A_ka_{1k}+b_{1k})u)]\\
&+C_8g_k[a_{2k}v-\tau((a_{1k}a_{2k}+d_{12k})uv+(a_{2k}^2+d_{22k})v^2+(A_ka_{2k}+b_{2k})v)]\\
&+C_7g_k[a_{2k}-\tau((a_{1k}a_{2k}+d_{12k})u+(a_{2k}^2+d_{22k})v+(A_ka_{2k}+b_{2k}))]y\\
&+\frac{1}{2}C_7g_k[(a_{1k}^2+d_{11k})(-ut)^2+2(a_{1k}a_{2k}+d_{12k})(-ut)(y-vt)+(a_{2k}^2+d_{22k})(y-vt)^2],
\end{aligned} \tag{2.8}$$

where g_k are the equilibrium states at both sides of the cell interface, and the coefficients $a_{1k},\cdots,A_k$ are defined according to the expansion of g_k.

After determining the kinetic part f_0, the equilibrium state g in the integral solution Eq. (2.5) are expanded in space and time consistent with f_0 as follows

$$\begin{aligned}
g = g_0 &+ \frac{\partial g_0}{\partial x}x + \frac{\partial g_0}{\partial y}y + \frac{\partial g_0}{\partial t}t + \frac{1}{2}\frac{\partial^2 g_0}{\partial x^2}x^2 + \frac{\partial^2 g_0}{\partial x\partial y}xy + \frac{1}{2}\frac{\partial^2 g_0}{\partial y^2}y^2\\
&+\frac{1}{2}\frac{\partial^2 g_0}{\partial t^2}t^2 + \frac{\partial^2 g_0}{\partial x\partial t}xt + \frac{\partial^2 g_0}{\partial y\partial t}yt,
\end{aligned} \tag{2.9}$$

where g_0 is the equilibrium state located at interface, which is determined through the compatibility condition Eq. (2.2)

$$\int \psi g_0 d\Xi = W_0 = \int_{u>0}\psi g_l d\Xi + \int_{u<0}\psi g_r d\Xi. \tag{2.10}$$

Substituting Eq. (2.9) into integral solution Eq. (2.5), the hydrodynamic part is written as

$$\begin{aligned}
&\frac{1}{\tau}\int_0^t g(x',y',t',u,v)e^{-(t-t')/\tau}dt' \\
=&C_1g_0+C_2g_0\overline{a}_1u+C_2g_0\overline{a}_2v+C_1g_0\overline{a}_2y+C_3g_0\overline{A} \\
&+\frac{1}{2}C_4g_0(\overline{a}_1^2+\overline{d}_{11})u^2+C_6g_0(\overline{A}\overline{a}_1+\overline{b}_1)u+\frac{1}{2}C_5g_0(\overline{A}^2+\overline{B}) \\
&+\frac{1}{2}C_1g_0(\overline{a}_2^2+\overline{d}_{22})y^2+C_2g_0(\overline{a}_2^2+\overline{d}_{22})vy+\frac{1}{2}C_4g_0(\overline{a}_2^2+\overline{d}_{22})v^2 \\
&+C_2g_0(\overline{a}_1\overline{a}_2+\overline{d}_{12})uy+C_4g_0(\overline{a}_1\overline{a}_2+\overline{d}_{12})uv \\
&+C_3g_0(\overline{A}\overline{a}_2+\overline{b}_2)y+C_6g_0(\overline{A}\overline{a}_2+\overline{b}_2)v,
\end{aligned} \tag{2.11}$$

where the coefficients $\overline{a}_1,\overline{a}_2,\cdots,\overline{A}$ and $\overline{B}$ are defined from the expansion of the equilibrium state g_0. The coefficients $C_i, i=1,\cdots,8$ in Eq. (2.11) and Eq. (2.8) are given by

$$\begin{aligned}
&C_1=1-e^{-t/\tau},\quad C_2=(t+\tau)e^{-t/\tau}-\tau,\quad C_3=t-\tau+\tau e^{-t/\tau},\quad C_4=-(t^2+2t\tau)e^{-t/\tau}, \\
&C_5=t^2-2t\tau,\quad C_6=-t\tau(1+e^{-t/\tau}),\quad C_7=e^{-t/\tau},C_8=-te^{-t/\tau}.
\end{aligned}$$

Thus, the gas distribution function at the cell interface is fully determined.

For the smooth flow, the polynomials at both sides of the cell interface take the same polynomial $\overline{W}(x)$, which gives $g_0=g_l=g_r$ and identical slopes. Consequently, the gas distribution function Eq. (2.5) reduces to the continuous one

$$\begin{aligned}
f=&g_0[1-\tau(\overline{a}_1u+\overline{a}_2v+\overline{A})] \\
&+g_0[\overline{a}_2-\tau((\overline{a}_1\overline{a}_2+\overline{d}_{12})u+(\overline{a}_2^2+\overline{d}_{22})v+(\overline{A}\overline{a}_2+\overline{b}_2))]y \\
&+g_0[\overline{A}-\tau((\overline{A}\overline{a}_1+\overline{b}_1)u+(\overline{A}\overline{a}_2+\overline{b}_2)v+(\overline{A}^2+\overline{B}))]t \\
&+g_0[\frac{1}{2}(\overline{a}_2^2+\overline{d}_{22})y^2+(\overline{A}\overline{a}_2+\overline{b}_2)yt+\frac{1}{2}(\overline{A}^2+\overline{B})t^2].
\end{aligned} \tag{2.12}$$

The superscripts or subscripts of the coefficients $a_1,a_2,\cdots,A,B$ in Eq. (2.8), Eq. (2.11) and Eq. (2.12) are omitted for simplicity and they are determined by the compatibility condition and the spatial derivatives of macroscopic flow variables, which will be introduced in the next section, as follows

$$\begin{cases}
\langle a_1\rangle=\dfrac{\partial W}{\partial x},\ \langle a_2\rangle=\dfrac{\partial W}{\partial y},\ \langle A+a_1u+a_2v\rangle=0, \\
\langle a_1^2+d_{11}\rangle=\dfrac{\partial^2 W}{\partial x^2},\ \langle a_2^2+d_{22}\rangle=\dfrac{\partial^2 W}{\partial y^2},\ \langle a_1a_2+d_{12}\rangle=\dfrac{\partial^2 W}{\partial x\partial y}, \\
\langle(a_1^2+d_{11})u+(a_1a_2+d_{12})v+(Aa_1+b_1)\rangle=0, \\
\langle(a_1a_2+d_{12})u+(a_2^2+d_{22})v+(Aa_2+b_2)\rangle=0, \\
\langle(Aa_1+b_1)u+(Aa_2+b_2)v+(A^2+B)\rangle=0,
\end{cases} \tag{2.13}$$

where $<\cdots>$ are the moments of gas distribution function, and defined by

$$<\cdots>=\int g(\cdots)\psi d\Xi.$$

3 Compact reconstruction

In the traditional high-order schemes, a high-order polynomial is reconstructed or updated inside each cell, and the exact Riemann solver [8] or approximate Riemann solvers [34] are used to provide flux function at the cell interface. The Riemann solver presents the Euler solution from two constant states, which has the wave propagation in the normal direction of the cell interface only. Due to its constant flux and state at the cell interface, the cell interface solution has only first-order accuracy, which can be hardly used in the reconstruction at the beginning of next time step. In the gas-kinetic scheme, besides the numerical fluxes, the pointwise values of the macroscopic variables at a cell interface can be obtained by taking moments of the gas distribution function [38] as well,

$$W_{i+1/2,j}(t,y)=\int \psi f(x_{i+1/2},y,t,u,v,\xi)d\Xi. \tag{3.1}$$

As shown in the last section, the whole curve of the polynomial of the macroscopic variables will participate the flow evolution, and the spatial and temporal derivatives of the gas distribution function are coupled nonlinearly. These pointwise values at the cell interface Eq. (3.1) are strong high-order dynamic solutions, which can be used in the reconstruction stage at the beginning of next time step. This is also the main point we would like to emphasize in this paper that the low order dynamics of the Riemann solver may be the bottle neck for the development of high-order compact numerical schemes. The use of the weak solution, such as DG, is mainly to avoid the use of high-order flow dynamics. In the following subsections, a third-order compact reconstruction will be presented for both one and two dimensional cases, in which the pointwise values at the cell interface and the cell averaged values in the neighboring cells only are used in the high-order reconstruction.

3.1 One-dimensional initial data reconstruction

In the one-dimensional case, the stencils of the compact reconstruction for cell I_i are shown in Fig. 1. Two types of stencils are considered in the reconstruction and the proce-

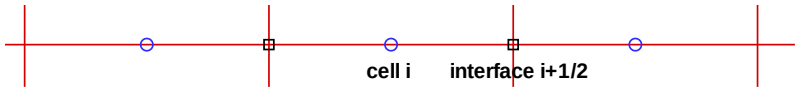

Figure 1: One dimensional stencil for the cell I_i. The circles represent the cell averaged values $\overline{W}_{i-1},\overline{W}_i,\overline{W}_{i+1}$ and the squares represent the pointwise values $W_{i-1/2},W_{i+1/2}$ at the cell interface.

dure are listed as follows:

1. For one-sided stencils $S_1=\{\overline{W}_{i-1},W_{i-1/2},\overline{W}_i\}$ and $S_2=\{\overline{W}_i,W_{i+1/2},\overline{W}_{i+1}\}$, two quadratic polynomials can be defined as $\phi_k(x)=\overline{W}_i+a_2^k x+a_3^k\omega_x,k=1,2$, where $\omega_x=\frac{1}{2}(x^2-\frac{1}{12}\Delta x^2)$. According to the cell averaged values $\overline{W}_{i+(-1)^k}$ and point values $W_{i+(-1)^k/2}$, the coefficients of ϕ_1 and ϕ_2 can be expressed as

$$\begin{aligned}&a_3^k=3(\overline{W}_i+\overline{W}_{i+(-1)^k}-2W_{i+(-1)^k/2}))/\Delta x^2,\\&a_2^k=(-1)^k[2(W_{i+(-1)^k/2}-\overline{W}_i)/\Delta x-a_3^k\Delta x/6]=(-1)^k(\widetilde{a}_2^k-a_3^k\Delta x/6).\end{aligned}$$

   To deal with possible flow with discontinuity, the above coefficients are limited as

$$\begin{cases}a_3=minmod\{a_3^1,a_3^2\},\\a_2=minmod\{-\widetilde{a}_2^1+a_3\Delta x/6,\widetilde{a}_2^2-a_3\Delta x/6\},\end{cases}\tag{3.2}$$

   where $minmod\{\cdot,\cdot\}$ is the minmod limiter. With these modified coefficients, the polynomial $W_1(x)=\overline{W}_i+a_2x+a_3\omega_x$ from two one-sided stencils can be fully determined.

2. For the central stencil $S_3=\{\overline{W}_{i-1},\overline{W}_i,\overline{W}_{i+1}\}$, the polynomial $W_2(x)$ can be obtained according to

$$\int_{I_{i-1}}W_2(x)dx=\overline{W}_{i-1},\quad\int_{I_{i+1}}W_2(x)dx=\overline{W}_{i+1}.$$

3. With the polynomials $W_i(x)$, i=1,2 corresponding to the one-sided and central stencils, the non-linear weights ω_i [17] are used to construct the combined polynomial in the cell I_i as follows

$$W(x)=\omega_1W_1(x)+\omega_2W_2(x),\tag{3.3}$$

   where $\omega_i=\frac{\alpha_i}{\sum_i\alpha_i}$, $\alpha_i=\frac{1}{(\varepsilon+I(W_i))^2}$, $\varepsilon=10^{-6}$ in computation and $I(W_i)$ is the smooth indicator of $W_i(x)$, which is expressed as

$$I(W_i)=\sum_{1\le l\le 2}\int_{I_i}h^{2l-1}(W_i^{(l)})^2dx,$$

   where $W_i^{(l)}$ is the l-th order derivative of W_i.

   In most cases, the polynomial $W_1(x)$ corresponding to the one-sided stencils can well resolve the discontinuities, and the central stencil is introduced to improve the accuracy in the smooth region. In the computation, the smooth indicator of W_1 directly takes $I(W_1)=Ch^2$. Thus, $I(W_2)=\mathcal{O}(1)$ in the region with discontinuity and W_1 is the dominant one in Eq. (3.3); in the smooth region, $I(W_2)=\mathcal{O}(h^2)$ and $W(x)$ is the average of $W_1(x)$ and $W_2(x)$.

3.2 Two-dimensional initial data reconstruction

Similar to the one-dimensional case, as shown in Fig. 2, two types of stencils are used in the data reconstruction, i.e. one-sided stencils and central stencil. For the cell I_{ij}, the quadratic polynomial $\phi_k(x,y)$ are defined by

$$\phi_k(x,y)=\overline{W}_{i,j}+a_2^k x+a_3^k y+a_4^k \omega_x+a_5^k \omega_y+a_6^k xy,$$

where $\overline{W}_{i,j}$ is the cell averaged value of I_{ij}. For the one-sided stencil 1, the polynomial $\phi_1(x,y)$ can be determined according to three cell averaged values and four pointwise values at Gaussian integration points as follows:

$$\begin{aligned}
&\int_{I_{i+1,j}} \phi_1(x,y)dxdy=\overline{W}_{i+1,j}, \quad \int_{I_{i,j+1}} \phi_1(x,y)dxdy=\overline{W}_{i,j+1},\\
&\phi_1(x_{i+\frac{1}{2}},y_{j+\frac{\sqrt{3}}{6}})=W_{i+\frac{1}{2},j^+}, \quad \phi_1(x_{i+\frac{1}{2}},y_{j-\frac{\sqrt{3}}{6}})=W_{i+\frac{1}{2},j^-},\\
&\phi_1(x_{i+\frac{\sqrt{3}}{6}},y_{j+\frac{1}{2}})=W_{i^+,j+\frac{1}{2}}, \quad \phi_1(x_{i-\frac{\sqrt{3}}{6}},y_{j+\frac{1}{2}})=W_{i^-,j+\frac{1}{2}}.
\end{aligned}$$

The least square solution for the above over-determined system are written as

$$\begin{cases}
a_4^1=3[(\overline{W}_{i,j}+\overline{W}_{i+1,j})-(W_{i+\frac{1}{2},j^+}+W_{i+\frac{1}{2},j^-})]/\Delta x^2,\\
a_2^1=(W_{i+\frac{1}{2},j^+}+W_{i+\frac{1}{2},j^-}-2\overline{W}_{ij})/\Delta x-a_4^1\Delta x/6,\\
a_5^1=3[(\overline{W}_{i,j}+\overline{W}_{i,j+1})-(W_{i^+,j+\frac{1}{2}}+W_{i^-,j+\frac{1}{2}})]/\Delta y^2,\\
a_3^1=(W_{i^+,j+\frac{1}{2}}+W_{i^-,j+\frac{1}{2}}-2\overline{W}_{ij})/\Delta y-a_5^1\Delta y/6,\\
a_6^1=\sqrt{3}[W_{i+\frac{1}{2},j^+}-W_{i+\frac{1}{2},j^-}+W_{i^+,j+\frac{1}{2}}-W_{i^-,j+\frac{1}{2}}]/\Delta x\Delta y-(a_2^1/\Delta y+a_3^1/\Delta x).
\end{cases} \tag{3.4}$$

Similarly, the coefficients a_m^k of the quadratic polynomials $\phi_k(x,y)$, k=2,3,4 and m=2,$\cdots$,6 corresponding to other three one-sided stencils can be also obtained.

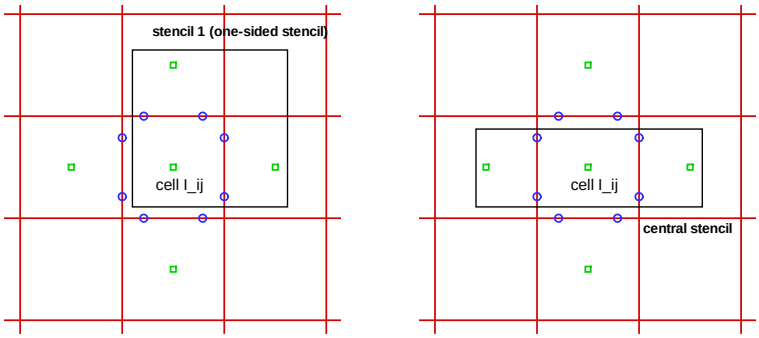

Figure 2: Two types of stencils for the compact reconstruction of cell I_{ij}. Left one has four one-sided stencils, where only stencil 1 is shown; the right one is the central stencil. The squares represent the cell averaged values of each cell; circles are the pointwise values at the Gaussian points, which can be obtained from the solution in Eq. (3.1).

Due to the decoupling of normal and tangential derivatives in Eq. (3.4) for the quadratic polynomial $\phi_k(x,y)$, the normal derivatives a_2,a_4 and tangential derivatives a_3,a_5 can be modified according to the limiter in Eq. (3.2), respectively. With the modified coefficients a_2,a_3, the cross derivative a_6^1 is modified as

$$\widetilde{a}_6^1=\sqrt{3}[W_{i+\frac{1}{2},j^+}-W_{i+\frac{1}{2},j^-}+W_{i^+,j+\frac{1}{2}}-W_{i^-,j+\frac{1}{2}}]/\Delta x\Delta y-(a_2/\Delta y+a_3/\Delta x).$$

Choosing the one with the smallest absolute value from $\widetilde{a}_6^k$, $k=1,\cdots,4$, the limiting procedure is done and a quadratic polynomial $W_1(x,y)=\overline{W}_{i,j}+a_2x+a_3y+a_4\omega_x+a_5\omega_y+a_6xy$ can be obtained for the four one-sided stencils.

For the central stencil S_5, the polynomial $W_2(x,y)$ can be obtained as follows:

$$\begin{aligned}
&\int_{I_{i-1}} W_2(x,y)dxdy=\overline{W}_{i-1}, \quad \int_{I_{i+1}} W_2(x,y)dxdy=\overline{W}_{i+1},\\
&W_2(x_{i+\frac{1}{2}},y_{j+\frac{\sqrt{3}}{6}})=W_{i+\frac{1}{2},j^+}, \quad W_2(x_{i+\frac{1}{2}},y_{j-\frac{\sqrt{3}}{6}})=W_{i+\frac{1}{2},j^-},\\
&W_2(x_{i-\frac{1}{2}},y_{j+\frac{\sqrt{3}}{6}})=W_{i-\frac{1}{2},j^+}, \quad W_2(x_{i-\frac{1}{2}},y_{j-\frac{\sqrt{3}}{6}})=W_{i-\frac{1}{2},j^-}.
\end{aligned}$$

With the non-linear weights for the two-dimensional reconstruction, the polynomial in the cell I_{ij} is constructed as

$$W(x,y)=\omega_1W_1(x,y)+\omega_2W_2(x,y),$$

where ω_i, $i=1,2$ are the non-linear weights and details can be found in [10].

3.3 Reconstruction for equilibrium part

In this subsection, a quadratic polynomial $\overline{W}(x,y)$ corresponding to equilibrium (hydrodynamic) part will be constructed, which is expressed as

$$\overline{W}(x,y)=W_0+b_2x+b_3y+\frac{1}{2}b_4x^2+\frac{1}{2}b_5y^2+b_6xy.$$

The conservative variables W_0 at the center of cell interface are obtained according to the compatibility condition Eq. (2.10), in which g_l and g_r are equilibrium states corresponding to the initially reconstructed conservative variables $W^l_{i,j+1/2}$,$W^r_{i,j+1/2}$ at both sides of cell interface.

To determine this polynomial with the compact stencils, six cell averaged values are used as shown in Fig. 3 with the following conditions

$$\iint_{I_{i+m,j+n}} \overline{W}(x,y)dxdy=\overline{W}_{i+m,j+n},$$

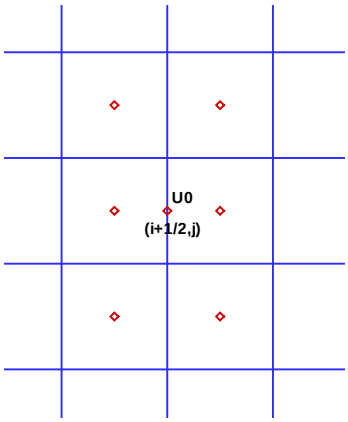

Figure 3: The stencil for the equilibrium distribution around the cell interface $(i+1/2,j)$.

where $m=0,1$, $n=-1,0,1$. The coefficients of $\overline{W}(x,y)$ can be obtained by the least square procedure, and they are expressed as

$$\begin{cases} b_2=((\overline{W}_{i+1,j+1}-\overline{W}_{i,j+1})+2(\overline{W}_{i+1,j}-\overline{W}_{ij})+(\overline{W}_{i+1,j-1}-\overline{W}_{i,j-1}))/4\Delta x, \\ b_3=(\overline{W}_{i+1,j+1}-\overline{W}_{i+1,j-1}+\overline{W}_{i,j+1}-\overline{W}_{i,j-1})/4\Delta y, \\ b_4=(26(\overline{W}_{i+1,j}+\overline{W}_{ij})-(\overline{W}_{i+1,j+1}+\overline{W}_{i,j+1}+\overline{W}_{i+1,j-1}+\overline{W}_{i,j-1})-48W_0)/8\Delta x^2, \\ b_5=(\overline{W}_{i+1,j+1}-2\overline{W}_{i+1,j}+\overline{W}_{i+1,j-1}+\overline{W}_{i,j+1}-2\overline{W}_{i,j}+\overline{W}_{i,j-1})/2\Delta y^2, \\ b_6=(\overline{W}_{i+1,j+1}-\overline{W}_{i,j+1}-\overline{W}_{i+1,j-1}+\overline{W}_{i,j-1})/2\Delta x\Delta y. \end{cases}$$

Similarly, the quadratic polynomial $\overline{W}(x)$ across the cell interface can be also constructed for the one-dimensional case.

Remark 3.1. In this section, a compact simple reconstruction is presented, which can be easily extended to unstructured mesh. Theoretically, for the third-order gas-kinetic scheme, three independent pointwise values at a cell interface Eq. (3.1) can be obtained and used for the spatial data reconstruction. There are many choices for the reconstruction. To obtain optimal and robust reconstruction scheme specifically to the kinetic formulation is an interesting open question and needs further investigation.

4 Numerical tests

In this section, numerical tests for both inviscid flow and viscous flow will be presented to validate our numerical scheme. For the inviscid flow, the collision time τ takes

$$\tau=\epsilon\Delta t+C|\frac{p_l-p_r}{p_l+p_r}|\Delta t,$$

where $\epsilon=0.05$ and $C=1$. For the viscous flow, we have

$$\tau=\frac{\mu}{p}+|\frac{p_l-p_r}{p_l+p_r}|\Delta t,$$

where p_l and p_r denotes the pressures on the left and right sides of the cell interface, μ is the viscous coefficient, and p is the pressure at the cell interface. In the smooth flow regions, it will reduce to $\tau=\mu/p$. For diatomic molecules with $\gamma=1.4$, the current gas-kinetic scheme solves the NS equations with the inclusion of bulk viscosity [42]. For monatomic gas with $\gamma=5/3$, there is no bulk viscosity involved. Δt is the time step which is determined according to the CFL condition. In the numerical tests, CFL number takes 0.2. Besides the last case, the uniform Cartesian meshes with $\Delta x=\Delta y$ are used.

For the smooth flow, the compact reconstruction is based on the conservative variables directly. For the flow with discontinuity, with $A_{i+1/2,j}=(\partial f/\partial W)_{W=W^*}$ for $f(W)=(\rho U,\rho U^2+p,\rho UV,U(\rho E+p))$ and $W^*=(W_{i,j}+W_{i+1,j})/2$, the cell averaged and point conservative values can be projected into the characteristic filed by $\omega=RW$, where R is the matrix corresponding to right eigenvectors of A. The compact reconstruction is applied on the characteristic variables ω. With the reconstructed polynomials for characteristic variables, the reconstructed conservative variables are determined by the inverse of projection.

4.1 Accuracy tests

We consider two test cases to verify the numerical order of the compact gas-kinetic scheme in comparison with the analytical solutions of Euler equations. The first case is the advection of density perturbation, and the initial condition is set as follows

$$\rho(x)=1+0.2\sin(\pi x),\quad U(x)=1,\quad p(x)=1,\quad x\in[0,2].$$

The periodic boundary condition is adopted and thus the analytic solution is

$$\rho(x,t)=1+0.2\sin(\pi(x-t)),\quad U(x,t)=1,\quad p(x,t)=1.$$

In the computation, the uniform mesh is used, and the L^1 and L^2 errors and orders at $t=2$ are presented in Table 1, which shows the third-order accuracy.

Table 1: Space accuracy test for the advection of density perturbation.

mesh	L^1 norm	order	L^2 norm	order
50	6.994400E-006		7.765728E-006	
100	7.925999E-007	3.141535	8.803306E-007	3.141004
200	1.069000E-007	2.890331	1.182243E-007	2.896518
400	1.329999E-008	3.006764	1.516575E-008	2.962638

The second one is the isotropic vortex propagation problem [30]. The mean flow is $(\rho,u,v,p)=(1,1,1,1)$, and an isotropic vortex is added to the mean flow, i.e., with perturbation in u,v and temperature $T=p/\rho$, and no perturbation in entropy $S=p/\rho^{\gamma}$. The perturbation is given by

$$(\delta u,\delta v)=\frac{\epsilon}{2\pi}e^{\frac{(1-r^2)}{2}}(-y,x),$$
$$\delta T=-\frac{(\gamma-1)\epsilon^2}{8\gamma\pi^2}e^{1-r^2},\quad \delta S=0,$$

where $r^2=x^2+y^2$ and the vortex strength $\epsilon=5$. The computational domain is $[-5,5]\times[-5,5]$, the periodic boundary conditions are imposed on the boundaries in both x and y directions, and uniform meshes are used. The exact solution is the perturbation which propagates with the velocity $(1,1)$. The L^1 and L^2 errors and orders at $t=10$ are presented in Table 2, which shows that the third-order accuracy can be also achieved.

Table 2: Accuracy test for the isotropic vortex propagation problem.

mesh	L^1 norm	order	L^2 norm	order
21×21	3.2800781E-02		6.2543898E-02	
41×41	5.5260700E-03	2.661948	9.4291484E-03	2.827986
81×81	8.7312283E-04	2.709969	1.5213625E-03	2.679191
121×121	2.6716280E-04	2.950650	4.8235722E-04	2.862094

4.2 One dimensional Riemann problem

The first one is Sod problem [33], the computational domain is $[0,1]$ and the ratio of specific heats takes $\gamma=1.4$. The initial condition is given by

$$(\rho,u,p)=\begin{cases}(1,0,1), & 0<x<0.5,\\ (0.125,0,0.1), & 0.5<x<1.\end{cases}$$

The density, velocity and pressure distributions with 100 mesh points and the exact solution at $t=0.2$ are given in Fig. 4, and the numerical results agree well with the exact solutions.

The second one is the Woodward-Colella blast wave problem [37]. The computational domain is $[0,100]$ with 400 uniform mesh points and with reflected boundary condition on both ends. The ratio of specific heats also takes $\gamma=1.4$. The initial condition is given as follows

$$(\rho,u,p)=\begin{cases}(1,0,1000), & 0\le x<10,\\ (1,0,0.01), & 10\le x<90,\\ (1,0,100), & 90\le x\le100.\end{cases}$$

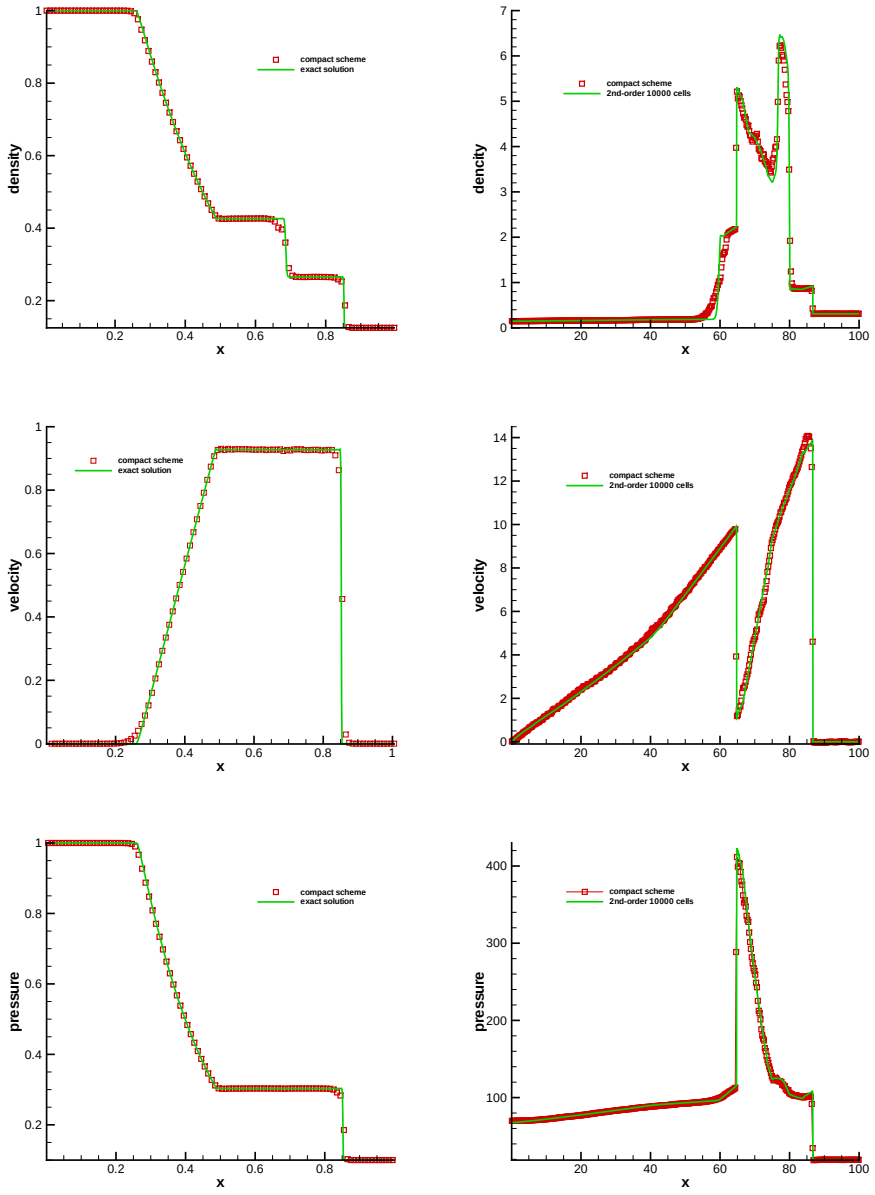

Figure 4: Sod problem (left): the density, velocity and pressure distributions at $t=0.2$. Blast wave problem (right): the density, velocity and pressure distributions at $t=3.8$.

The density, velocity and pressure distributions at t=3.8 are presented in Fig. 4, which are compared with the reference solutions obtained by the second-order BGK scheme with van Leer limiter. The figures show that the scheme can well resolve the strong shock and contact discontinuities, particularly for the local extreme values.

4.3 Two dimensional Riemann problem

In this case, two 2-D Riemann problems are tested to verify the capability in capturing complex two dimensional wave configurations. Both cases were presented in [21]. The computational domain is $[0,1]\times[0,1]$ and $\gamma=1.4$. The initial condition for the first case is

$$(\rho,u,v,p)=\begin{cases}(0.5313,0,0,0.4), & x>0.5,\ y>0.5,\\ (1,0.7276,0,1), & x<0.5,\ y>0.5,\\ (0.8,0,0,1), & x<0.5,\ y<0.5,\\ (1,0,0.7276,1), & x>0.5,\ y<0.5.\end{cases}$$

The initial condition for the second case is

$$(\rho,u,v,p)=\begin{cases}(1,0.75,-0.5,1), & x>0.5,\ y>0.5,\\ (2,0.75,0.5,1), & x<0.5,\ y>0.5,\\ (1,-0.75,0.5,1), & x<0.5,\ y<0.5,\\ (3.,-0.75,-0.5,1), & x>0.5,\ y<0.5.\end{cases}$$

Non-reflecting boundary conditions are used in x and y directions in the computation. The density distributions at $t=0.2$ shown in Fig. 5 for these cases with 200×200 and

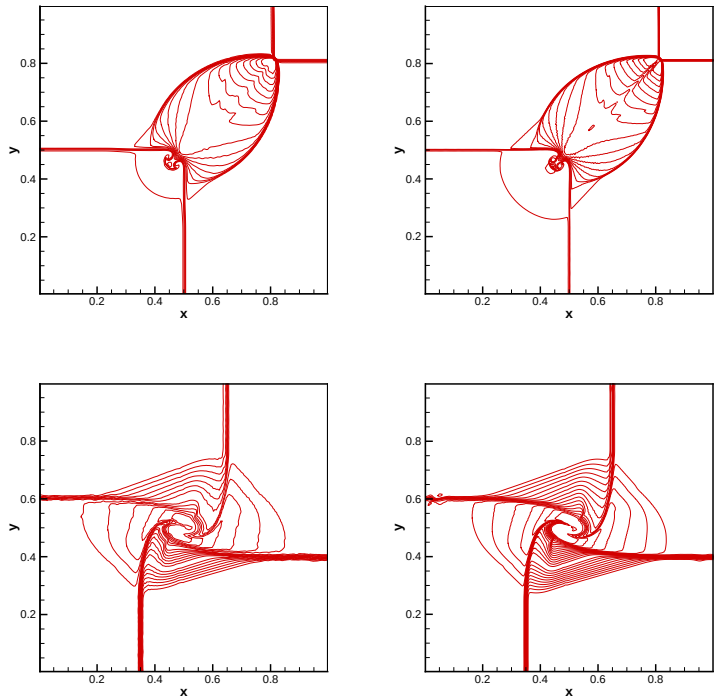

Figure 5: Two-dimensional Riemann problem for case 1 (top) and case 2 (bottom): the density distributions at $t=0.2$. Left: 200×200 cells; right: 400×400 cells.

400×400 uniform mesh points, and the results show that the current scheme well resolve the flow structure. With the refinement of mesh, the waves are sharply resolved, and the mushroom cap for the first Riemann problem is crisply captured.

4.4 Shock vortex interaction

This model problem describes the interaction between a stationary shock and a vortex for the inviscid flow, which was presented in [17]. The computational domain is taken to be $[0,2]\times[0,1]$. A stationary Mach 1.1 shock is positioned at $x=0.5$ and normal to the x-axis. The left upstream state is $(\rho,u,v,p)=(Ma^2,\sqrt{\gamma},0,1)$, where $\gamma=1.4$ is the specific heat ratio and Ma is the Mach number. A small vortex is obtained through a perturbation on the mean flow with the velocity (u,v), temperature $T=p/\rho$ and entropy $S=\ln(p/\rho^\gamma)$, and the perturbation is expressed as

$$(\delta u,\delta v)=\kappa\eta e^{\mu(1-\eta^2)}(\sin\theta,-\cos\theta),$$
$$\delta T=-\frac{(\gamma-1)\kappa^2}{4\mu\gamma}e^{2\mu(1-\eta^2)},\quad \delta S=0,$$

where $\eta=r/r_c$, $r=\sqrt{(x-x_c)^2+(y-y_c)^2}$, $(x_c,y_c)=(0.25,0.5)$ is the center of the vortex. κ indicates the strength of the vortex, μ controls the decay rate of the vortex, and r_c is the critical radius for which the vortex has the maximum strength. In the computation, $\kappa=0.3$, $\mu=0.204$ and $r_c=0.05$. The reflected boundary conditions are used on the top and bottom boundaries. The pressure distributions with 201×101 mesh points at $t=0.35$, 0.6 and 0.8 are shown in Fig. 6. By $t=0.8$, one branch of the shock bifurcations has reached the top boundary and been reflected, and the reflection is well captured. The detailed density distribution along the center horizontal line with 201×101, 401×201 and 801×401 uniform mesh points at $t=0.8$ are shown in Fig. 7.

4.5 Double Mach reflection problem

This problem was extensively studied by Woodward and Colella [37] for the inviscid flow. The computational domain is $[0,4]\times[0,1]$, and a solid wall lies at the bottom of the computational domain starting from $x=1/6$. Initially a right-moving Mach 10 shock is positioned at $(x,y)=(1/6,0)$, and tilted a 60° angle with the x-axis. The initial pre-shock and post-shock conditions are

$$(\rho,U,V,p)=(8,4.125\sqrt{3},-4.125,116.5),$$
$$(\rho,U,V,p)=(1.4,0,0,1).$$

The reflective boundary condition is used at the wall, while for the rest of bottom boundary, the exact post-shock condition is imposed. At the top boundary, the flow values are set to describe the exact motion of the Mach 10 shock. The density distributions with 400×100 and 800×200 uniform mesh points at $t=0.2$ are shown in Fig. 8. The current compact scheme resolves the flow structure under the triple Mach stem clearly.

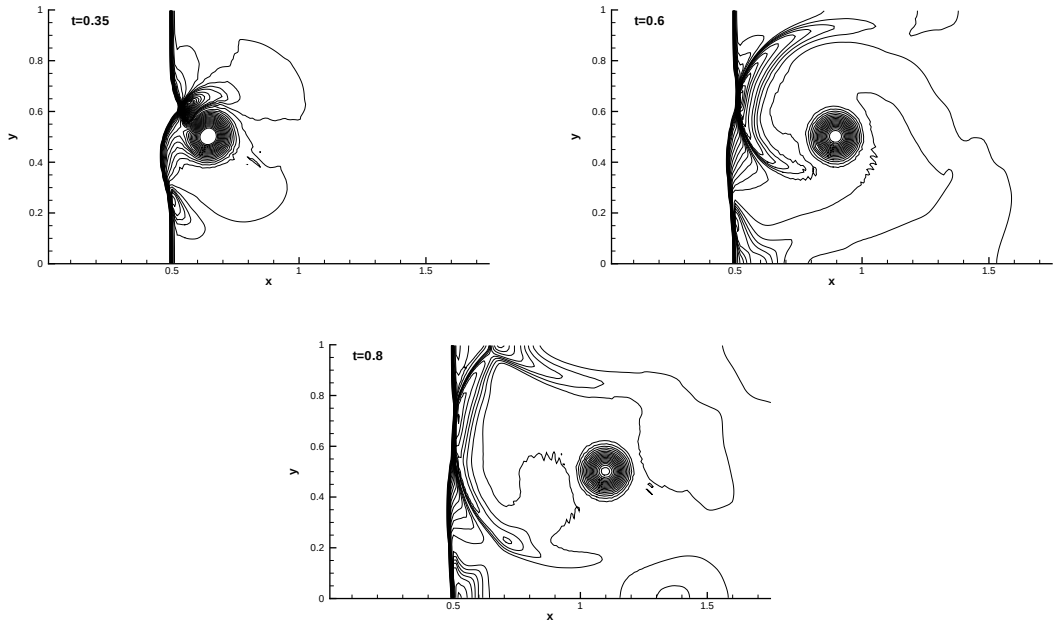

Figure 6: The pressure distribution for two-dimensional shock vortex interaction at $t=0.35,0.6$ and 0.8 with 201×101 uniform mesh points.

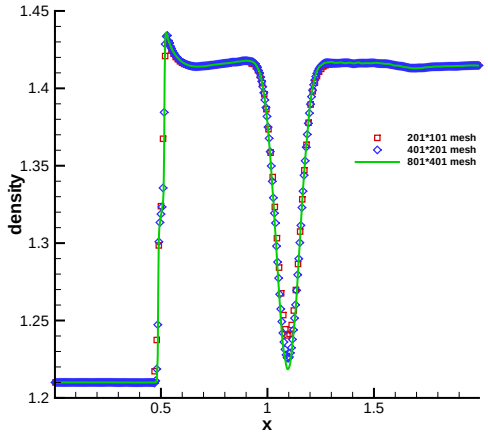

Figure 7: The density distribution for two-dimensional shock vortex interaction at $t=0.8$ along the horizontal symmetric line $y=0.5$ with 201×101, 401×201 and 801×401 uniform mesh points.

4.6 Front step problem

The front step problem was again studied extensively by Woodward and Colella [37] for the inviscid flow. The computational domain $[0,3]\times[0,1]$. The step is located at $x=0.6$

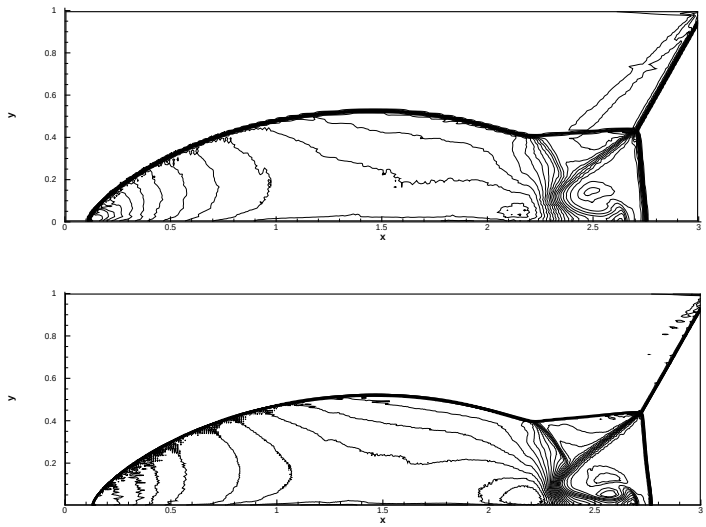

Figure 8: The density distributions of double mach reflection problem with the cell size $\Delta x=\Delta y=1/100$ (top) and $\Delta x=\Delta y=1/200$ (bottom) at $t=0.2$.

with height 0.2 in the tunnel. Initially, a right-going Mach 3 flow is used. Reflective boundary conditions are used along the walls of the tunnel, and inflow and outflow boundary conditions are used at the entrance and the exit. The corner of the step is center of a rarefaction fan, hence it is a singularity point. Without any special treatment around this point, the flow will be affected by the erroneous entropy layer. To minimize the numerical error generated at the corner of the step, the flow variables around the corner are modified according to [37]. Four cells starting from the corner in the first row above the step, and the first two cells in the 2nd row are modified. The densities are reset so that the entropy has same value as in cell just to the left and below the corner of step, and the magnitudes of the velocities are also reset so that the sum of enthalpy and kinetic energy of unit mass has the same value as in same cell used to reset entropy. The density distributions with 120×40, 240×80 and 360×120 uniform mesh points are presented at $t=4$ in Fig. 9.

4.7 Viscous shock tube problem

This problem was introduced in [6, 32] to test the performances of different schemes for viscous flows. In this case, an ideal gas is at rest in a two-dimensional unit box $[0,1]\times[0,1]$. A membrane located at $x=0.5$ separates two different states of the gas and the dimensionless initial states are

$$(\rho,u,p)=\begin{cases}(120,0,120/\gamma), & 0<x<0.5,\\ (1.2,0,1.2/\gamma), & 0.5<x<1,\end{cases}$$

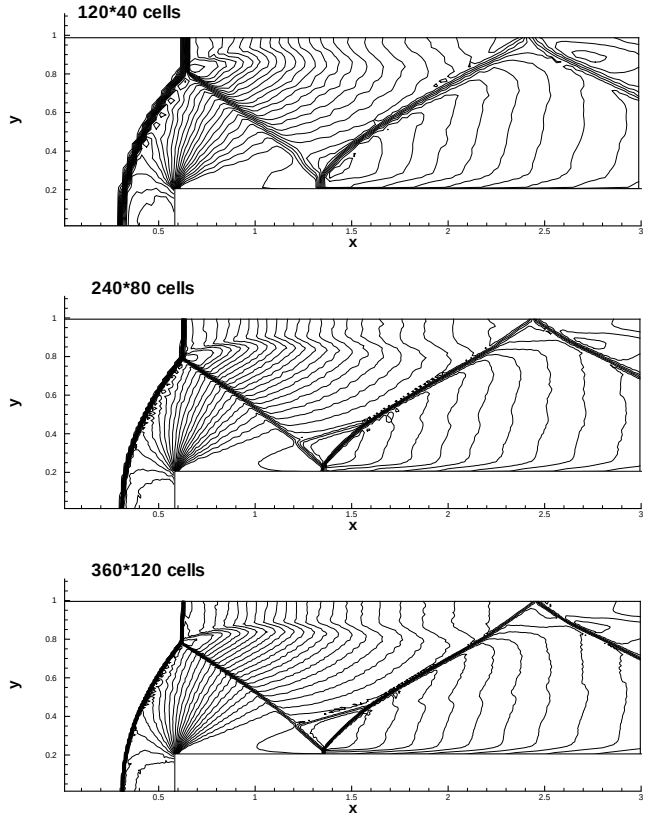

Figure 9: The density distribution of the front step problem with 120×40, 240×80 and 360×120 mesh points for the inviscid flow at $t=4$.

where $\gamma=1.4$ and Prandtl number $Pr=0.73$.

The membrane is removed at time zero and wave interaction occurs. A shock wave, followed by a contact discontinuity, moves to the right with Mach number $Ma=2.37$ and reflects at the right end wall. After the reflection, it interacts with the contact discontinuity. The contact discontinuity and shock wave interact with the horizontal wall and create a thin boundary layer during their propagation. The solution will develop complex two-dimensional shock/shear/boundary-layer interactions. This case is tested in the computational domain $[0,1]\times[0,0.5]$, a symmetrical condition is used on the top boundary $x\in[0,1], y=0.5$ and non-slip boundary condition and adiabatic condition for temperature are imposed at solid wall boundaries. The density distribution for $Re=200$ at $t=1$ with 300×150 uniform mesh points is shown in Fig. 10. The complexity of the flow structure increases as the Reynolds number increases. The density distribution at $t=1$ with 600×300 and 1200×600 mesh points for $Re=1000$ are shown in Fig. 11. The current scheme can well resolve the complex flow structure. The density profiles along the lower wall for $Re=1000$ are also presented in Fig. 12.

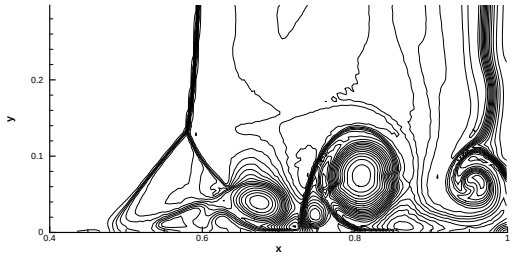

Figure 10: Reflected shock-boundary layer interaction. The density distribution at $t=1$ with 300×150 mesh points for $Re=200$.

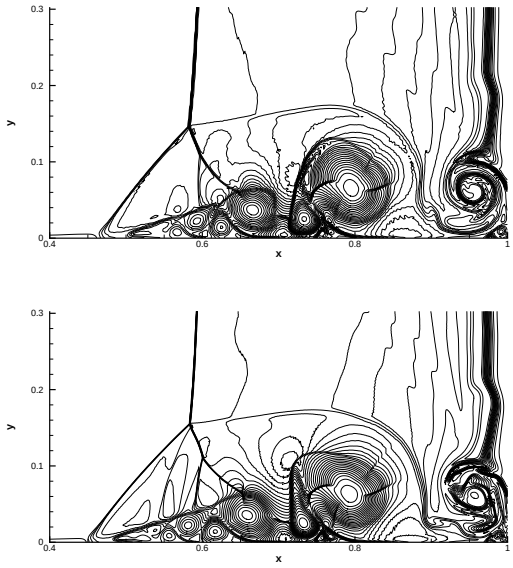

Figure 11: Reflected shock-boundary layer interaction. The density distribution at $t=1$ with 600×300 (top) and 1200×600 (bottom) mesh points for $Re=1000$.

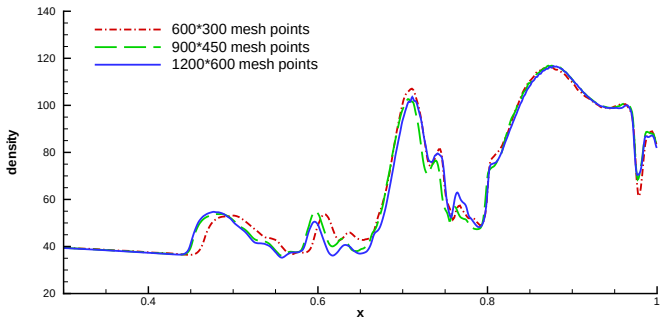

Figure 12: Reflected shock-boundary layer interaction. The density distribution at $t=1$ along the lower wall with $600\times300,900\times450,1200\times600$ mesh points for $Re=1000$.

4.8 Lid-driven cavity flow

The lid-driven cavity problem is one of the most important benchmarks for validating incompressible or low speed Navier-Stokes flow solvers. The fluid is bounded by a unit square and driven by a uniform translation of the top boundary. In this case, the flow is simulated with Mach number $Ma=0.15$ and $\gamma=5/3$ in the computational domain $[0,1]\times[0,1]$ and all boundaries are isothermal and nonslip. Numerical simulations are conducted for three Reynolds numbers $Re=400,1000$ and 3200. The streamlines for $Re=1000$ using 65×65 uniform mesh points are shown in Fig. 13. The results of U-velocities along the center vertical line, V-velocities along the center horizontal line and the benchmark data [7] are shown in Fig. 14 for $Re=1000$ and Fig. 15 for $Re=3200,400$. The simulation results match well with the benchmark data.

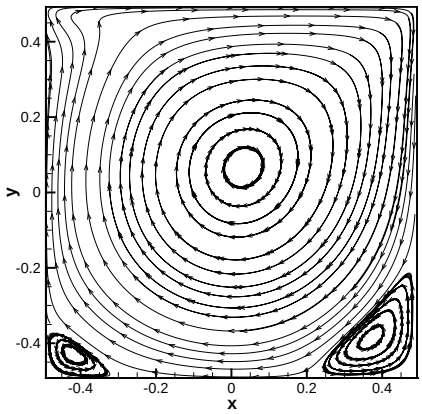

Figure 13: The streamlines for the cavity flow by 65×65 mesh points for $Re=1000$.

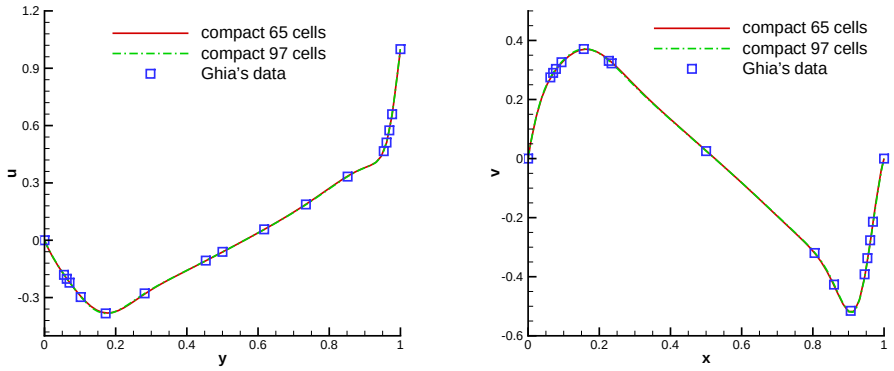

Figure 14: Lid-driven cavity flow: U-velocities along vertical centerline line (left) and V-velocities along horizontal centerline for $Re=1000$ with 65×65 and 97×97 mesh points. The reference data is from [7].

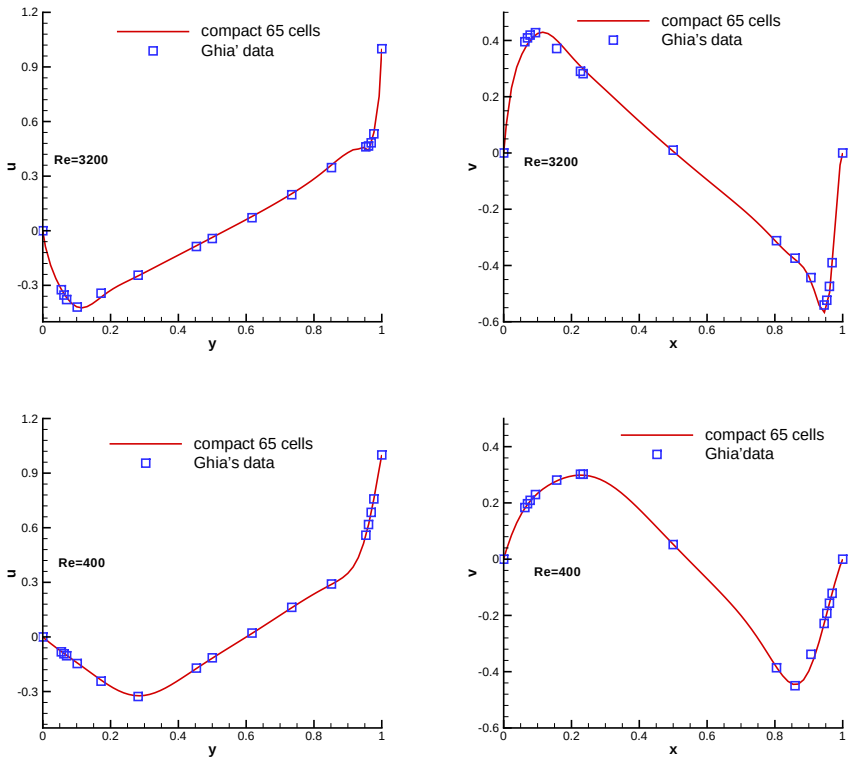

Figure 15: Lid-driven cavity flow: U-velocities along vertical centerline line (left) and V-velocities along horizontal centerline for $Re=3200$ and 400 with 65×65 mesh points. The reference data is from [7].

The lid-driven polar cavity flow is also tested under the curvilinear coordinate. The schematic diagram and the computational mesh for this case are given in Fig. 16. The computational domain in the polar coordinate (r,θ) takes $[1,2]\times[-0.5,0.5]$, and 65×65 uniform mesh points in the polar coordinate are used. The inner curved wall rotates anticlockwise with $Ma=0.15$. The flow pattern of this problem is governed by the Reynolds number defined as $Re=U_iR_i/\mu=350$, where U_i is the inner azimuthal velocity. All the boundaries are also isothermal and nonslip. The steady-state streamlines are presented in Fig. 16. The angular and radial velocity profiles along the horizontal line with $\theta=0$ are shown in Fig. 17 together with Fuchs' results [11]. Good agreement has been achieved between the current results and the benchmark data.

5 Conclusion

In this paper, a third-order compact gas-kinetic scheme is proposed for both inviscid and viscous flow simulations. The merit of the current kinetic scheme is that a high-order gas

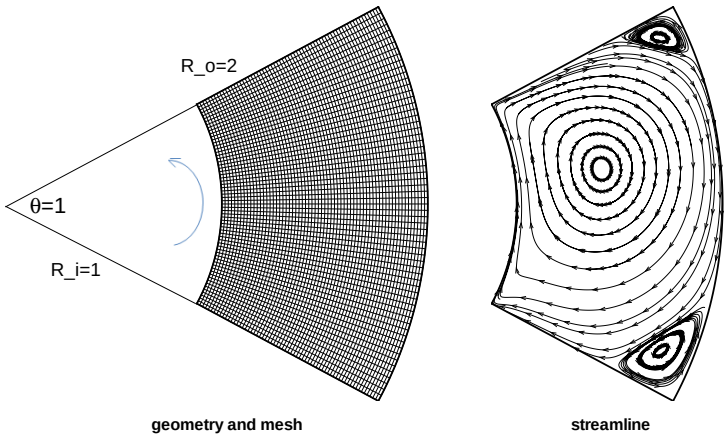

Figure 16: The schematic diagram (left) and steady-state streamline profile (right) for the polar cavity flow.

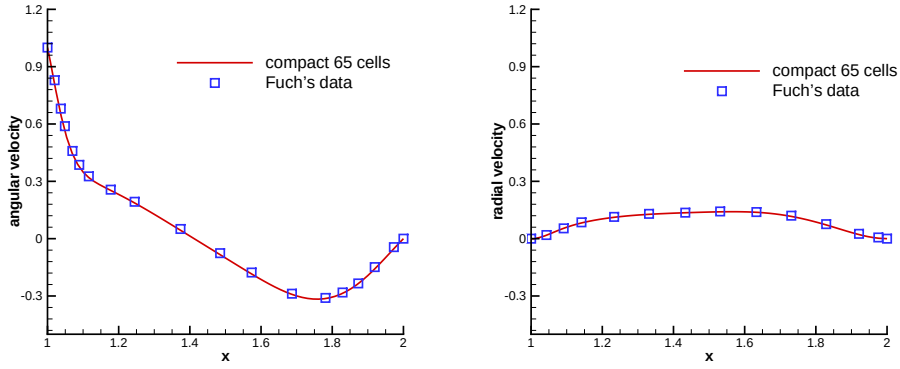

Figure 17: The profiles of angular velocity and radical velocity along the horizontal centerline with $\theta=0$ for the polar cavity flow and the reference data is taken from Fuchs [11].

evolution model is constructed and used for the evaluation of numerical fluxes and the pointwise flow variables at a cell interface. This can be only achieved with high-order gas evolution model because the solution at the cell interface at the next time level is a high accurate strong solution of the governing equations. Therefore, with the inclusion of the updated cell interface values, the scheme can be designed compactly. This can be hardly achieved for the schemes based on the Riemann solution. Therefore, other compact schemes, such as DG, are constructed based on the weak formulation. Physically, there may have intrinsic inconsistency between the first-order flow dynamics in the Riemann solution and the high-order flow solver with compact stencil. The weakness in the Riemann dynamics in the traditional ENO and WENO schemes are compensated through the large stencils. For example, the high-order derivatives are constructed from the data in the neighboring and neighboring cells in ENO formulation, instead of updated in the

compact DG scheme. Therefore, the compact DG formulation theoretically needs a high-order gas evolution solution, which couples the spatial and temporal evolution of flow variables compactly. The weak formulation, which supplies the lost dynamics in the Riemann solver, will be problematic in the regions with discontinuities. This is probably the reason that the DG can get failed for the flow simulation with shocks and complicated flow interactions. In smooth regions, any governing equation can be manipulated correctly in a physically consistent way, such as all kinds of equivalent weak formulations [14, 15].

In the current compact gas-kinetic scheme, both numerical fluxes and pointwise values are used in the construction of the numerical flow evolution. The core of the scheme is the use of the strong solution of the governing equation from an initial high-order reconstruction. Different from the traditional upwind and central schemes, the kinetic formulation is multidimensional, inviscid and viscous terms coupling, and has multi-scale evolution process from the kinetic to the hydrodynamic in the flux construction. This transition in different scale physics is equivalent to the transition from the initial upwind scheme to the final central difference one. In the current scheme, due to the high-order accuracy in space and time, the flux transport along a cell interface within a time step can be integrated analytically. The third-order kinetic scheme doesn't need to use Gaussian points flux integration and the Runge-Kutta time stepping. This scheme has been validated through the computations for the flows from the smooth incompressible to the hypersonic viscous interaction. Due to the high-order dynamics in the gas-kinetic formulation, more information can be extracted at the cell interface. How to use these information is an interesting research topic for the development of high-order schemes.

Acknowledgments

The current work was supported by Hong Kong research grant council (620813, 16211014) and HKUST (IRS15SC29, SBI14SC11).

References

[1] P.L. Bhatnagar, E.P. Gross, M. Krook, A Model for Collision Processes in Gases I: Small Amplitude Processes in Charged and Neutral One-Component Systems, Phys. Rev. 94 (1954) 511-525.
[2] C. Cercignani, The Boltzmann Equation and its Applications, Springer-Verlag, (1988).
[3] S. Chapman, T.G. Cowling, The Mathematical theory of Non-Uniform Gases, third edition, Cambridge University Press, (1990).
[4] B. Cockburn, C. W. Shu, TVB Runge-Kutta local projection discontinuous Galerkin finite element method for conservation laws II: general framework, Mathematics of Computation, 52 (1989) 411-435.
[5] B. Cockburn, C. W. Shu, The Runge-Kutta discontinuous Galerkin method for conservation laws V: multidimensional systems, J. Comput. Phys. 141 (1998), 199-224.
[6] V. Daru, C. Tenaud, High order one-step monotonicity-preserving schemes for unsteady compressible flow calculations, J. Comput. Phys. 193 (2004) 563-594.

[7] U. Ghia, K. N. Ghia, C.T Shin, High-Re solutions for incompressible flow using the Navier-Stokes equations and a multigrid method, J. Comput. Phys. 48 (1982) 387-411.
[8] S. K. Godunov, A difference scheme for numerical computation of discontinuous solution of hyperbolic equation, Math. Sbornik. 47 (1959) 271-306.
[9] A. Harten, B. Engquist, S. Osher and S. R. Chakravarthy. Uniformly high order accurate essentially non-oscillatory schemes, III. J. Comput. Phys. 71 (1987) 231-303.
[10] O. Friedrich, Weighted essentially non-oscillatory schemes for the interpolation of mean values on unstructured grids, J. Comput. Phys. 144 (1998) 194-212.
[11] L. Fuchs, N. Tillmark, Numerical and experimental study of driven flow in a polar cavity, International Journal for Numerical Methods in Fluids. 5 (1985) 311-329.
[12] H. Gao and Z.J. Wang, A high-order lifting collocation penalty formulation for the Navier-Stokes equations on 2D mixed grids, AIAA Paper 2009 3784.
[13] Z.L. Guo, K. Xu, and R.J. Wang, Discrete unified gas kinetic scheme for all Knudsen number flows: Low-speed isothermal case, Physical Review E 88, 033305 (2013).
[14] H.T. Huynh, A flux reconstruction approach to high-order schemes including discontinuous Galerkin methods, AIAA Paper (2007) 4079.
[15] H.T. Huynh, A reconstruction approach to high-order schemes including discontinuous Galerkin for diffusion, AIAA Paper (2009) 403.
[16] J. Jiang, Y.H. Qian, Implicit gas-kinetic BGK scheme with multigrid for 3D stationary transonic high-Reynolds number flows, Computers & Fluids. 66 (2012) 21-28.
[17] G.S. Jiang, C. W. Shu, Efficient implementation of Weighted ENO schemes, J. Comput. Phys. 126 (1996) 202-228.
[18] C. Jin, K. Xu, A unified moving grid gas-kinetic method in Eulerian space for viscous flow computation, J. Comput. Phys. 222 (2007) 155-175.
[19] G. Kumar, S.S. Girimaji, J. Kerimo, WENO-enhanced gas-kinetic scheme for direct simulations of compressible transition and turbulence, J. Comput. Phys. 234 (2013) 499-523.
[20] Q. Li, K. Xu, S. Fu, A high-order gas-kinetic Navier-Stokes flow solver, J. Comput. Phys. 229 (2010) 6715-6731.
[21] X.D. Liu, P.D. Lax, Solution of two-dimensional Riemann problems of gas dynamics by positive schemes, SIAM J. Sci. Comput. 19 (1998) 319-340.
[22] X.D. Liu, S. Osher, T. Chan, Weighted essentially non-oscillatory schemes, J. Comput. Phys. 115 (1994) 200-212.
[23] Y. Liu, M. Vinokur, Z.J. Wang, Spectral difference method for unstructured grids I: Basic formulation, J. Comput. Phys. 216 (2006) 780-801.
[24] J. Luo, L.J. Xuan, K. Xu, Comparison of fifth-order WENO scheme and WENO-gas-kinetic scheme for inviscid and viscous flow simulation, Commun. Comput. Phys. 14 (2013) 599-620.
[25] J. Luo, K. Xu, A high-order multidimensional gas-kinetic scheme for hydrodynamic equations, SCIENCE CHINA Technological Sciences, 56 (2013) 2370-2384.
[26] L. Mieussens, On the asymptotic preserving property of the unified gas-kinetic scheme for the diffusion limit of linear kinetic models, J. Comput. Phys. 253 (2013) 138-156.
[27] T. Ohwada, K. Xu, The kinetic scheme for full Burnett equations, J. Comput. Phys. 201 (2004) 315-332.
[28] L. Pan, K. Xu, Generalized coordinate transformation and gas-kinetic scheme, J. Comput. Phys. 287 (2015) 207-225.
[29] W.H. Reed, T.R. Hill, Triangular mesh methods for the neutron transport equation, Technical Report LA-UR-73-479, 1973, Los Alamos Scientific Laboratory, Los Alamos.
[30] C.W. Shu, Essentially non-oscillatory and weighted essentially non-oscillatory schemes for

hyperbolic conservation laws, Lecture Notes in Mathematics, Springer, 1998.
[31] C.W. Shu, S. Osher, Efficient implementation of essentially non-oscillatory shock capturing schemes, J. Comput. Phys. 77 (1988) 439-471.
[32] B. Sjögreen, H.C. Yee, Grid convergence of high order methods for multiscale complex unsteady viscous compressible flows, J. Comput. Phys. 185 (2003) 1-26.
[33] G.A. Sod, A survey of several finite difference methods for systems of nonlinear hyperbolic conservation laws, J. Comput. Phys. 27 (1978) 1-31.
[34] E. Toro, Riemann Solvers and Numerical Methods for Fluid Dynamics, Springer, (1997).
[35] Z.J. Wang, Spectral (finite) volume method for conservation laws on unstructured grids: basic formulation, J. Comput. Phys. 178 (2002) 210-251.
[36] Z.J. Wang, H. Gao, A unifying lifting collocation penalty formulation including the discontinuous Galerkin, spectral volume/difference methods for conservation laws on mixed grids, J. Comput. Phys. 228 (2009) 8161-8186
[37] P. Woodward, P. Colella, The numerical simulation of two dimensional fluids with strong shock, J. Comput. Phys. 54 (1984) 115-173.
[38] K. Xu, A Slope-update Scheme for Compressible Flow Simulation, J. Comput. Phys. 178 (2002) 252-259.
[39] K. Xu, Direct Modeling for Computational Fluid Dynamics: Construction and Application of Unified Gas-kinetic Schemes, World Scientific, (2015).
[40] K. Xu, A gas-kinetic BGK scheme for the Navier-Stokes equations and its connection with artificial dissipation and Godunov method, J. Comput. Phys. 171 (2001) 289-335.
[41] K. Xu and J. Huang, A unified gas-kinetic scheme for continuum and rarefied flows, J. Comput. Phys. 229 (2010) 7747-7764.
[42] K. Xu, H. Liu, J. Jiang, Multiple temperature kinetic model for continuum and near continuum flows, Physics of Fluids, 19 (2007) 016101.
[43] L.M. Yang, C. Shu, J. Wu, N. Zhao, Z.L. Lu, Circular function-based gas-kinetic scheme for simulation of inviscid compressible flows, J. Comput. Phys. 255 (2013) 540-557.